Journal of Materials Chemistry A



PAPER

View Article Online
View Journal | View Issue



Cite this: J. Mater. Chem. A, 2025, 13, 33528

On the cation distribution in acceptor doped Ba(Zr,Ce)O₃-(Zr,Ce)O₂ co-ionic composite electrolytes

Composite co-ionic ceramic electrolytes that combine proton and oxide ion conductors hold potential for co-electrolysis of CO2 and H2O for syngas production due to flexible control of the transport numbers of the two charge carriers. Contrary to purely oxide ion co-electrolysis, co-ionic co-electrolysis embodies the supply of CO2 and H2O separately to the negative and positive electrodes, respectively. This study focuses on the development of a chemically stable co-ionic composite electrolyte of an acceptor-doped Ba(Zr,Ce) O₃ proton conducting perovskite phase and an acceptor-doped (Ce,Zr)O₂ oxide ion conducting fluorite phase, annealed at temperatures between 800 and 1600 °C. Comprehensive evaluations of the composites' microstructure, hydration, and conductivity were performed, revealing that annealing temperature and cation selection significantly impact the properties and performance of co-ionic electrolytes. Higher annealing temperatures drive cation redistribution, with the perovskite phase becoming zirconium-rich at its B-site and depleted in acceptor dopants, resulting in diminished hydration and protonic conductivity. Herein, we show that composites pairing cerium-rich fluorite phases (e.g., Ce_{0.8}Gd_{0.2}O_{1.9}, CGO20, or Ce_{0.8}Y_{0.2}O_{1.9}, CYO20) display markedly improved performance. The BaCe_{0.8}Y_{0.2}O_{2.9} (BCY20)-CYO20 system (1:1 weight ratio) achieved the highest conductivity ($\sigma =$ 0.01 Scm⁻¹ at 650 °C in wet Ar), establishing itself as a promising candidate for co-ionic electrolyte applications in solid oxide electrochemical cells.

Received 6th April 2025 Accepted 27th August 2025

DOI: 10.1039/d5ta02711j

rsc.li/materials-a

Introduction

Charge and mass transfer in solid oxide electrochemical cells (SOECs) based on an electrolyte possessing both oxide ion and proton conductivity – hereafter referred to as a co-ionic electrolyte – offers unique operational possibilities from a theoretical point of view. In these materials, protons (H^+) and oxide ions (O^{2-}) can simultaneously counter-migrate across the electrolyte under an applied voltage between the electrodes. This configuration promotes water formation in fuel cell mode and water splitting in electrolysis mode at both electrodes. Co-ionic electrolytes have been reported to reduce concentration overpotentials at the electrodes, thereby improving Faraday efficiency. Moreover, co-ionic electrolytes offer an interesting possibility to co-electrolyse CO_2 and H_2O supplied to different electrodes (Fig. 1) to form dry syngas ($CO + H_2$) on the CO_2 side. 6,7

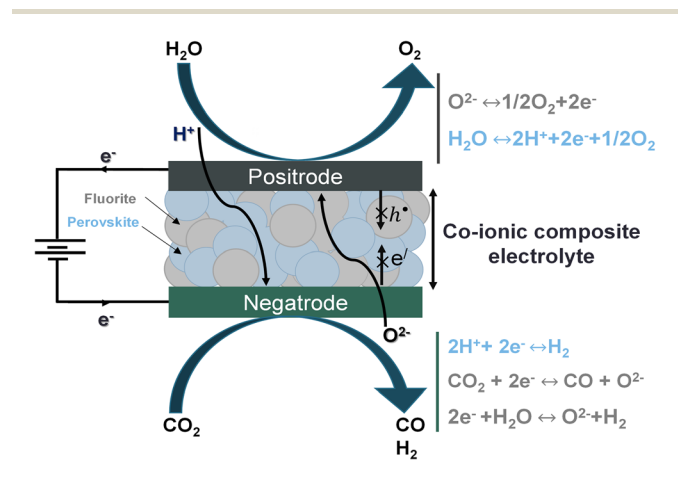


Fig. 1 Diagram illustrating syngas production mechanism using a coionic composite electrolyte in SOECs. Grey and blue spheres represent the counter-migration of protons (H⁺) and oxide ions (O²⁻), respectively. The term "positrode" refers to the steam electrode, while "negatrode" denotes the fuel electrode. Depending on volume fractions, the fluorite phase obstructs the p-type electronic conductivity (h') pathway somewhat, while the perovskite phase obstructs n-type electronic conductivity (e'), thereby helping to lower electronic leakage through the electrolyte.

^aCentre for Materials Science and Nanotechnology, Department of Chemistry, University of Oslo, P. O. Box 1033 Blindern, NO-0315 Oslo, Norway. E-mail: truls. norby@kjemi.uio.no

^bInstituto de Tecnología Química, Universitat Politècnica de València-Consejo Superior de Investigaciones Científicas, Av. Los Naranjos s/n, 46022 Valencia, Spain

Materials Physics, SINTEF Industry, Forskningsveien 1, NO-0373 Oslo, Norway

Coexistence of protons and oxygen vacancies in single-phase perovskite oxides results in mixed proton and oxide-ion conductivity with comparable transport numbers under conditions of partial hydration.3 In these perovskites, proton conductivity dominates at lower operating temperatures due to the exothermic hydration reaction. Iwahara et al.3 demonstrated that for 5-15 mol% Sm-doped BaCeO₃, the proton transport number in wet atmospheres approaches unity at temperatures below 650 °C. The enthalpy of hydration varies with the Zr to Ce ratio in acceptor-doped BaZr_{1-x}Ce_xO₃,8 with proton transport numbers potentially being lower in Zr-rich compositions, though still remaining above 0.9 below 600 °C at $pH_2O \approx 0.026$ atm.9,10 This suggests that single-phase perovskite oxides may not be suitable as co-ionic electrolytes at intermediate temperatures (450-600 °C) if nearly equal proton and oxide ion transport number is required. Although proton conductivity has been reported for fluorite oxides, their proton transport numbers are typically too low to serve as co-ionic electrolytes. 11

To overcome the limitations of single-phase materials, composites - where protons and oxide ions migrate through distinct phases - offer an alternative. The coexistence of fluorite- and perovskite-based electrolyte phases is demonstrated by X-ray diffraction even after sintering at high temperatures (1300-1650 °C).12-14 These composites may provide better control over the overall transport numbers and are less dependent on operating conditions. Zhao et al.15 showed that the proton transport number for a BaCe_{0.5}Zr_{0.4}Y_{0.1}O_{3-δ}- $Ce_{0.5}Y_{0.5}O_{2-\delta}$ composite electrolyte is 0.5 and 0.25 for 2:1 and 1:1 mole ratios, respectively, at $T \sim 650$ °C in wet reducing atmospheres. Furthermore, it is shown that composite electrolytes may reduce the electronic losses typically observed in ceriabased electrolytes under reducing conditions.16-18 Additionally, the sintering temperature for these composites can be lower than that required for state-of-the-art proton conductors, such as yttrium-doped barium zirconate (BZY).19 The potential advantages of co-ionic composites come at a cost of the two partial conductivities somewhat reduced by percolation restrictions, expectedly to 25% for a 50:50 randomly packed dense composite.

As shown in Table S1, there is a significant variation in conductivity compared to single-phase fluorite-based and perovskite-based electrolytes. This may arise from cation interdiffusion between the fluorite and perovskite phases during high-temperature sintering. Studies show that there is a strong tendency for cations to migrate from the perovskite phase to the fluorite phase at elevated sintering temperatures, leading to significant depletion of the proton conducting phase.5,20 Cation interdiffusion at the interface of composite positrodes or electrolytes composed of either two perovskites or two fluorites may also be a critical issue during hightemperature sintering and the operation of electrochemical cells.21,22

Thermogravimetric analysis of hydration is a robust method for quantifying the effective acceptor concentration in proton conducting electrolytes 16,23,24 and in the present work, we predict the effective acceptor concentration within the proton conducting phase of composite co-ionic electrolytes after annealing by analysing the hydration behaviour of acceptordoped BaZr_{1-x}Ce_xO₃ (BZC). We consider that the oxide-ion conducting fluorite phase exhibits negligible hydration. Through comprehensive analyses of hydration, element composition, and conductivity, we investigate the cation distribution between acceptor-doped BZC and Zr_{1-v}Ce_vO₂ composites. Various compositions with different concentrations of Zr, Ce, Gd, Sc, and Y were studied with annealing temperatures between 800 and 1600 °C. Two synthesis approaches were employed: solid-state reactive sintering (SSRS), where cations freely partition between phases during composite formation, and solid-state sintering (SSR), where pre-sintered phases are annealed at high temperature, with the possibility of interdiffusion. Our findings reveal significant variations in dopant distribution across the composite electrolytes, resulting in conductivity differences of several orders of magnitude.

2. **Experimental**

2.1. Materials synthesis

2.1.1 Single phase proton and oxide-ion conducting electrolytes. Various proton and oxide-ion conducting electrolytes were prepared for this study. Proton conducting electrolytes included $BaCe_{0.8}Y_{0.2}O_{2.9}$ (BCY20), BaZr_{0.4}Ce_{0.4}Y_{0.2}O_{2.9} (BZCY442), BaZr_{0.8}Y_{0.2}O_{2.9} (BZY20) and BaZr_{0.8}Sc_{0.2}O_{2.9} (BZS20), synthesized using solid-state reactive sintering (SSRS) or spraypyrolysis methods. Oxide-ion conducting electrolytes consisted of Ce_{0.8}Y_{0.2}O_{1.9} (CYO20), Ce_{0.8}Gd_{0.1}Y_{0.1}O_{1.9} (CGY1010), Ce_{0.7}- $Gd_{0.1}Y_{0.2}O_{1.85}$ (CGY1020), and $Ce_{0.6}Gd_{0.1}Y_{0.3}O_{1.8}$ (CGY1030), prepared using the solid-state reaction (SSR). Commercial powders such as 8YSZ (TZ-8Y, Tosoh, Japan) and Ce_{0.8}Gd_{0.2}O_{1.9} (CGO20, 99.9%, Alfa Aesar, USA) were also included. For conductivity measurements of these single-phase materials, pellets were sintered in ambient air at 1600-1650 °C for 10 hours yielding relative density >90%. Further details on fabrication protocols and compositions are provided in the SI, Section SI-2.

2.1.2 Composite materials. The BaO-CeO₂-ZrO₂ mixture in 1:1:1 molar ratio was fabricated by mixing BaCO₃, CeO₂ and ZrO₂ (purity >99%, Alfa Aesar, USA) and then pelletised and sintered at 1500 °C for 50 h.

To examine the cation distribution between two phases, we prepared a BaZr_{0.8}Y_{0.1}Yb_{0.1}O₃ (BZYYb811)-CGO20 composite electrolyte using the SSRS method. Precursor powders corresponding to the nominal composition were prepared by ball milling BaCO₃, ZrO₂, CeO₂, Y₂O₃, Yb₂O₃, and Gd₂O₃ (purity ≥99.9%, Sigma-Aldrich) with zirconia balls in ethanol (absolute, VWR) for 72 hours. The resulting mixtures were dried at 120 °C while stirring on a hotplate, pressed into pellets, and reaction sintered at 1500 °C for 10 hours (Table 1).

Additionally, a composite electrolyte using solid-state reaction (SSR) was fabricated where a proton conducting electrolyte (BCY20, BZCY442, BZY20 or BZS20) was mixed with an oxide ion conducting electrolyte (CYO20, CGO20, or 8YSZ) in a 1:1 weight ratio. Initially, the powders of each single-phase material were ground using a mortar and pestle and then sieved to obtain particles with sizes ranging from 32 to 64 μm . The resulting

Table 1 The weight, mole, and volume ratios, along with synthesis methods for the composite materials used in this study. SSRS refers to one-step solid-state reactive sintering, and SSR to solid-state reaction. The $BaZrO_3-CeO_2$ and BZYYb811-CGO20 composites were synthesised based on their mole ratios, with the weight and volume ratios subsequently calculated. For all other composites, mixing was carried out using weight ratios, and both mole and volume ratios were calculated

Composite materials	Weight ratio	Mole ratio	Volume ratio	Synthesis method/T sintering
BaZrO ₃ -CeO ₂	1.61:1	1:1	65.3:34.6	SSRS/1500 °C
BZYYb811-CGO20	1.63:1		65.9:34.1	
BCY20 + CYO20	1:1	1:1.96	53.8:46.2	SSR/(800 °C to 1600 °C)
BCY20-CGO20		1:1.81	53.5:46.5	
BCY20 + 8YSZ		1:2.26	49.1:50.9	
BZCY442-CYO20		1:1.84	54.2:45.8	
BZCY442-8YSZ		1:2.11	49.5:50.5	
BZY20-CYO20		1:72	54.6:45.4	
BZY20-8YSZ		1:98	49.9:50.1	
BZS20-CYO20		1:71		

mixtures were then mixed with a binder using a mortar and pestle. Pellets were pressed from the powder mixture and sintered at temperatures ranging from 800 °C to 1600 °C (Table 1).

2.2. Structural, thermal, and electrical analyses

Microstructural, phase, thermal, and electrical analyses were carried out using scanning electron microscopy with energy-dispersive X-ray spectroscopy (SEM/EDS), scanning transmission electron microscopy (STEM), laboratory and synchrotron X-ray diffraction (XRD), thermogravimetric analysis (TG), and impedance spectroscopy; detailed experimental procedures are provided in the SI.

Results and discussion

The electrical conductivity of BZCY442-1NiO, derived from impedance spectroscopy, is presented as a function of temperature in humid Ar (Fig. 2) and as a function of oxygen partial pressure ($p(O_2)$) every 50° from 550 to 750 °C in humidified gas (SI Fig. S1). In addition to the measured data points, the fitted lines for partial proton (σ_{H^+}) and oxide-ion conductivity ($\sigma_{O^{2-}}$), as well as the corresponding proton transport number (t_{H^+}), are displayed in Fig. 2 (see SI Table S2 for thermodynamic and transport parameters).

The data in Fig. 2 reflect the typical behaviour of a high temperature proton conductor. Protons are the predominating charge carriers at low temperatures, gradually levelling off on increasing temperature (\sim 600 °C) as the proton concentration decreases due to dehydration (cf. Fig. 4). At higher temperature, the electrical conductivity increases again, reflecting oxide-ion conduction. The proton transport number at intermediate temperatures (400–600 °C) exceeds 0.9.

Fig. S1 shows that the total conductivity represents primarily $p(O_2)$ -independent ionic conductivity at low and intermediate $p(O_2)$ and approaches a $p(O_2)^{1/4}$ dependency at high $p(O_2)$ due to an increasing contribution of p-type electronic conduction.^{25,26}

Fig. 3 similarly displays the conductivity of ceria in wet nitrogen as a function of varying levels of yttrium and/or gadolinium substitution, ranging from 20 to 40 mol%. It has been reported that the practical solubility limit for yttrium or

gadolinium in ceria is approximately 40 mol% without the formation of secondary phases. 27,28 It has been shown in the literature that the conductivity of 20% acceptor-substituted ceria at intermediate oxygen partial pressures (wet N₂, $p(O_2)\sim 10^{-5}$ atm) is primarily by oxide ions. 29 The conductivity of acceptor substituted ceria reaches a maximum with respect to the acceptor concentration, which has been interpreted to reflect increasing defect interactions and lattice distortions. 29,30

These fluorites do not hydrate to any extent, but chemisorbed and physisorbed water have been reported to result in surface protonic conductivity for porous, fine-grained ceria and yttria, ³¹ introducing distinct features at low and intermediate temperatures in Arrhenius representations of the electrical conductivity. The conductivity in Fig. 3 does, however, not exhibit any such features.

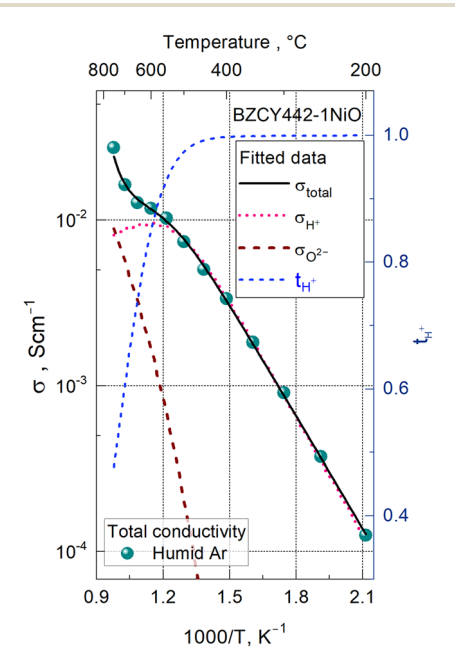


Fig. 2 DC conductivity and proton transport number of BZCY442+1NiO as a function of temperature in humid Ar. The hydration data and modelling of electrical conductivity are detailed in the SI.

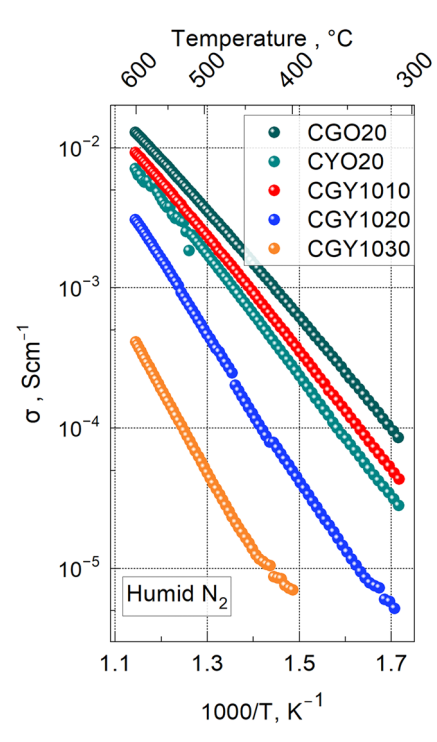


Fig. 3 DC conductivity of acceptor-substituted CeO₂ as a function of temperature in humid N₂.

The behaviour of the electrical conductivity of the perovskite and fluorites in Fig. 2 and 3, respectively, underscores the need for a composite to reach high co-ionic conductivity at intermediate temperatures, with nearly equal proton and oxide ion transport numbers. In BZCY single-phase materials, ambipolar co-ionic conductivity is influenced by the Zr/Ce ratio and remains low in Ce-rich perovskites, particularly at intermediate temperatures (Fig. S2, SI).

In the following sections we present results of, and discuss how, interdiffusion of cations degrades the conductivity characteristics of composites based on these materials. However, to justify various key points of the discussion, we firstly outline some aspects of the single-phase proton and oxide-ion conductors.

3.1. Single phase electrolytes

The XRD results of the BCY20, BZCY442, BZY20, and BZS20 proton conducting electrolytes are shown in SI Fig. S3, with the corresponding structural parameters summarised in Table 2. All four materials were confirmed to be single-phase, indicating the formation of a solid solution between the cerate and zirconate.25,32

Fig. 4 presents the proton concentration of the BCY20, BZCY442, BZY20, and BZS20 in wet air as a function of temperature from 800 to 200 °C. The proton concentration increases as the temperature decreases, reaching saturation below approximately 400 °C, reflecting the exothermic nature of the hydration reaction. The extracted thermodynamic values are summarised in SI Table S3. Based on the proton concentration, the effective acceptor concentrations are 19.4 mol% and

19.2 mol% for BCY20 and BZCY442, respectively, essentially matching the nominal 20 mol%. In contrast, BZY20 and BZS20 show a lower effective acceptor concentration of 14.5 mol% and 9.1 mol%, respectively. As the zirconium content increases, the hydration enthalpy becomes less negative, consistent with literature reports.³³ This trend may be attributed to the reduced electronegativity difference between the A- and B-site cations in the ABO₃ perovskite structure.³⁴⁻³⁶ The reason for the low effective acceptor concentration in BZY20 and BZS20 is unclear; however, the presence of secondary phases is unlikely to be the cause, as synchrotron XRD analysis of BZY20 reveals only minor amounts of secondary phases (<0.5 wt%), comparable to those in BZCY442 (SI Fig. S7).

The XRD analysis of the CYO20 material sintered at 1650 °C, is presented in SI Fig. S4, with the corresponding structural parameters detailed in Table 2.

3.2. Composite co-ionic electrolytes

3.2.1 Cation distribution in the composite electrolytes made by SSRS. Fig. 5 presents the results of XRD and SEM-EDS for BaO-CeO₂-ZrO₂ mixtures (1:1:1 mole ratio) sintered at 1500 °C for 50 hours. Rietveld refinement (Fig. 5) confirmed the formation of perovskite BaZrO3-based and fluorite CeO2-based phases (Table 2) and no BaCeO3-based phase, which was supported by EDS analysis showing only the two separate phases (Fig. 5b-e). This result is in accordance with tabulated thermodynamic values since the formation enthalpy of BaZrO₃ (-120.0 kJ mol⁻¹) is more negative than that of BaCeO₃ (-45.8 kJ mol⁻¹).37,38

Based on the above results, we aimed to synthesise a co-ionic electrolyte by introducing acceptor dopants according to the nominal composition BZYYb811-CGO20 (1:1 mol ratio) via the SSRS route at 1500 °C. The selection of different acceptor dopants (Y, Yb, Gd) was aimed at revealing their preferred site distribution in the composite system, as the SSRS method allows them to freely redistribute toward equilibrium.

Fig. 6 presents STEM-EDS observations of the product from this experiment. An EDS spectrum and a line scan across two grains are provided in SI Fig. S8. Semi-quantitative analysis of the EDS data revealed that, instead of the intended composite, the perovskite phase is BaZr_{0.6}Ce_{0.34}(Y,Yb,Gd)_{0.04}O₃, while the fluorite composition is $Ce_{0.51}(Y,Yb,Gd)_{0.49}O_2$. Consequently, Y, Yb, and Gd primarily dissolved in the CeO₂ phase, leading to excessive doping of the CeO2 fluorite phase and negligible doping levels in the BaZrO₃-based phase. From the perspective of co-ionic conductivity, this composition results in poor oxideion conductivity in the fluorite phase due to the negative effects of high doping levels (as illustrated in Fig. 3) and significantly reduced proton conductivity in the perovskite phase because of the low acceptor concentration.

3.2.2 Cation distribution in the composite co-ionic electrolyte made by SSR. Co-ionic composites were also synthesised by SSR: mixing single-phase BCY20 with different acceptor substituted fluorite compositions: CYO20, CGO20, and 8YSZ, all sintered at 1600 °C. The XRD results from these syntheses are shown in SI Fig. S5, with refined unit cell parameters

Table 2 Crystal structures, lattice parameters, and refinement details from XRD data for single-phase and composite materials

	Perovskite phase		Fluorite phase		
Composition	Space group	Lattice parameters (Å)	Space group	Lattice parameters (Å)	R _{wp} (%)
BaZrO ₃ /PDF 01-074-1299	$Pm\bar{3}m$	4.1815	_	_	_
BaCeO ₃ /PDF 01-074-1299	Pmcn	a = 8.7790	_	_	_
		b = 6.2140			
		c = 6.2360			
CeO ₂ /PDF 01-080-8533	_	_	$Fm\bar{3}m$	5.4073	_
$Ce_{0.8}Gd_{0.2}O_{1.9}/PDF$ 01-075-0162	_	_	$Fm\bar{3}m$	5.4230	_
8YSZ PDF 00-030-1468	_	_	$Fm\bar{3}m$	5.1390	_
CYO20	_	_	$Fm\bar{3}m$	5.4041	8.6
BCY20	$R\bar{3}c$	a = 6.2191	_	_	11.3
		c = 15.1902			
	I2/m	a = 6.2532			
		b = 8.7399			
		c = 6.2452			
BZCY442	$Pm\bar{3}m$	4.3101	_	_	20
BZY20	$Pm\bar{3}m$	4.2351	_	_	21.1
BZS20	$Pm\bar{3}m$	4.1956	_	_	_
BaZrO ₃ -CeO ₂	$Pm\bar{3}m$	4.1958	$Fm\bar{3}m$	5.4037	20.9
BCY20-CYO20	$R\bar{3}c$	a = 6.2182	$Fm\bar{3}m$	5.4044	13.1
		c = 15.0313			
	I2/m	a = 6.1963			
		b = 8.6946			
		c = 6.1978			
BCY20-CGO20	$R\bar{3}c$	a = 6.2130	$Fm\bar{3}m$	5.4190	7.3
		c = 15.2194			
	I2/m	a = 6.2104			
		b = 8.8123			
		c = 6.2101			
BCY20-8YSZ	Pm3m	4.1928	$Fm\overline{3}m$	5.2599	21.9

summarised in Table 2. All XRD patterns show only the presence of two phases: perovskite and fluorite.

It is noted that the crystal symmetry of $BaCe_{1-x}Y_xO_{3-\alpha}$ varies with Y content and could serve as an indicator for the yttrium acceptor concentration in the perovskite phase.³⁹⁻⁴¹ For x < 0.1, $BaCe_{1-x}Y_xO_{3-\alpha}$ generally crystallizes in an orthorhombic perovskite structure with the space group *Pnma* at room temperature, ^{41,42} as shown in Table 2 for $BaCeO_3$. The x = 0.15 composition contains monoclinic (I2/m) and orthorhombic (Incn) phases.^{41,42} For x = 0.2 (BCY20), when sintered in ambient air, rhombohedral ($R\overline{3}c$) and monoclinic (I2/m) crystal

structures coexist. 40,41 This aligns with the results presented in SI Fig. S3.

For the BCY20–CYO20 mixture, the lattice parameter of the CYO phase (5.4039 Å) is slightly smaller than that of nominal CYO20 (5.4041 Å), suggesting that the yttrium content in the fluorite is higher than the original 20 mol%. BCY appears to retain both rhombohedral ($R\bar{3}c$) and monoclinic (I2/m) crystal structures with a decrease in lattice parameters relative to BCY20. Based on the differences in ionic radii, this indicates that Y³⁺ ions have been replaced by Ce⁴⁺ ions. In future studies it would be useful to investigate potential compositional

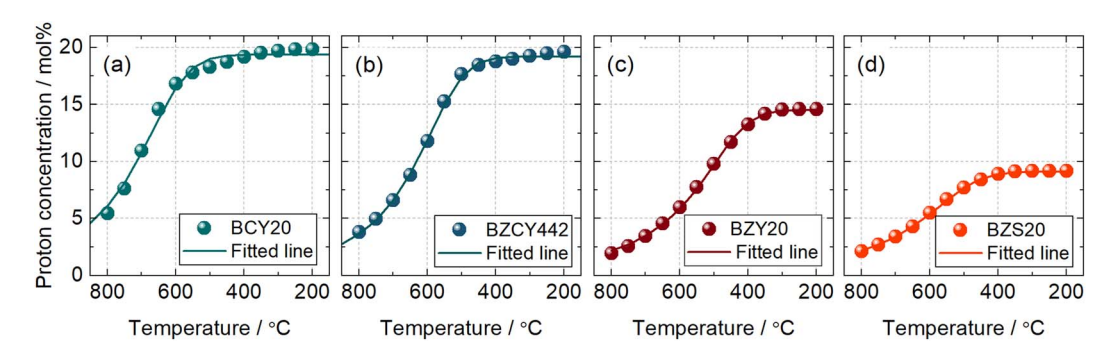


Fig. 4 Proton concentration of BCY20 (sintered at 1650 °C) (a), BZCY442 (1600 °C) (b), BZY20 (1600 °C) (c) and BZS20 (1650 °C) (d) measured by TG in the temperature range 200–800 °C in wet air.

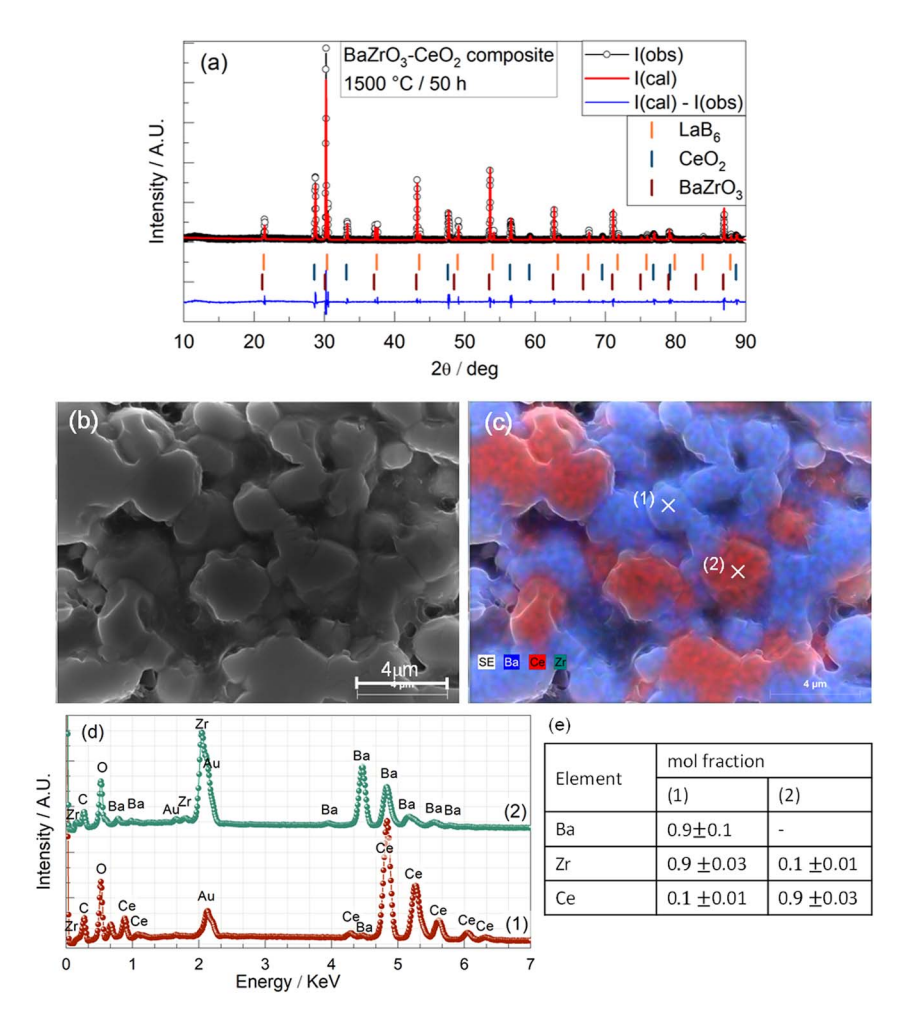


Fig. 5 Characterization of BaZrO₃-CeO₂ (1:1 mol ratio) composite electrolytes synthesised using the SSRS method at 1500 °C for 50 hours: XRD patterns (a), SEM image (b), EDS mapping (c), EDS spectrum (d) and EDS compositional analysis (e) for points (1) and (2) in image (c). Stoichiometries are normalised such that the molar fractions of Zr + Ce sum to 1 for each phase

differences between the rhombohedral and monoclinic phases in BCY20.

A similar trend of decreasing lattice parameters is also observed for the BCY phase in the nominal BCY20-CGO20 mixture (Table 2). The lattice parameter of the resulting fluorite phase (5.4190 Å) is smaller compared to single-phase CGO20 (5.4230 Å), indicating diffusion of yttrium into CGO. However, it can be concluded that the yttrium content in BCY for both the BCY20-CYO20 and BCY20-CGO20 composites remains >15 mol%, as both the rhombohedral and monoclinic crystal structures are present.40,41

When the fluorite phase is instead 8YSZ, the crystal structure of BCY20 undergoes a significant transformation during annealing of the BCY20-8YSZ nominal composite at 1600 °C, shifting to a cubic structure (cf. SI Fig. S6). It has been reported that the crystal symmetry in $BaCe_{1-x}Zr_xY_{0.2}O_{3-\alpha}$ increases with increasing zirconium content, exhibiting a cubic structure for x ≥ 0.4.43 Accordingly, a substantial substitution of cerium with zirconium has occurred.

The cation distributions in the BCY20-CYO20 and BCY20-8YSZ composite electrolytes are depicted in Fig. 7 and 8. Both

composites exhibit two distinct phases: a barium-rich phase and a cerium/zirconium-rich phase, consistent with the XRD results shown in SI Fig. S4. EDS results reveal a noticeable difference in yttrium distribution between the two compositions. In BCY20-CYO20, BCY contains a moderate amount of yttrium (~13 atom%), while for BCY20-8YSZ, yttrium is virtually absent in BCY. In the BCY20-8YSZ composite, there is substantial inter-diffusion between the two phases, giving notable amounts of cerium in the fluorite phase, and transforming BCY20 to essentially undoped BCZ. This observation is in accordance with XRD results, which show a cubic structure in the perovskite phase (SI Fig. S6).

3.2.3 Thermogravimetric analysis of composite co-ionic electrolytes from SSR. With this background on phase formation and nominal compositions of the co ionic composites, we use proton uptake to elucidate variations in their effective acceptor concentration. The TG curves and relative densities are provided in the SI (Fig. S11 and S12).

Fig. 9a illustrates the effective acceptor concentration of nominal BCY20 in composites with CYO20, CGO20, and 8YSZ as the oxide ion conducting phase. When sintered at 800 °C, the

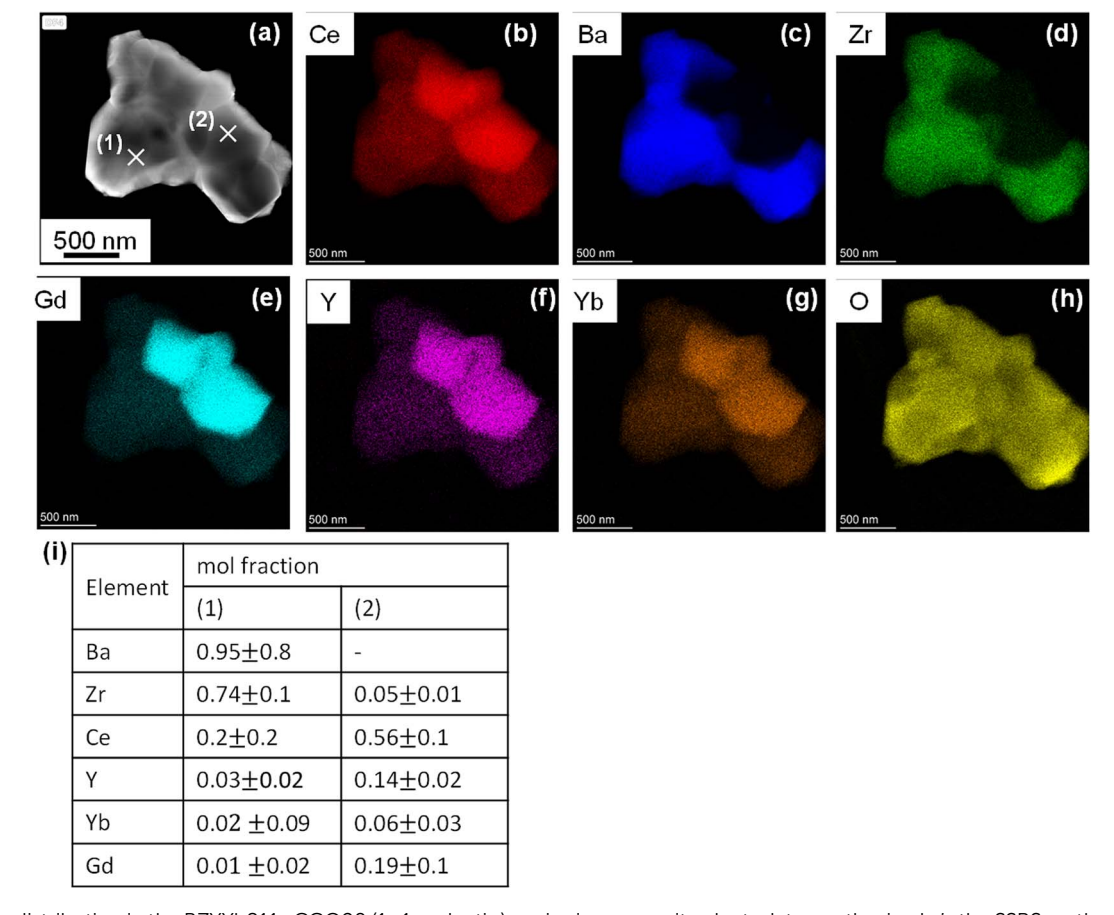


Fig. 6 Cation distribution in the BZYYb811-CGO20 (1:1 mol ratio) co-ionic composite electrolyte, synthesised *via* the SSRS method, analysed by STEM/EDS: annular dark field image (a) and EDS maps (b-h) are shown, along with the semi-quantitative analysis of the cations (i) for points (1) and (2) in image (a). Stoichiometries are normalised such that atomic fractions of Zr + Ce + Y + Yb sum to 1 for both the perovskite and fluorite phases. For fabrication methods and phase ratios, see Table 1.

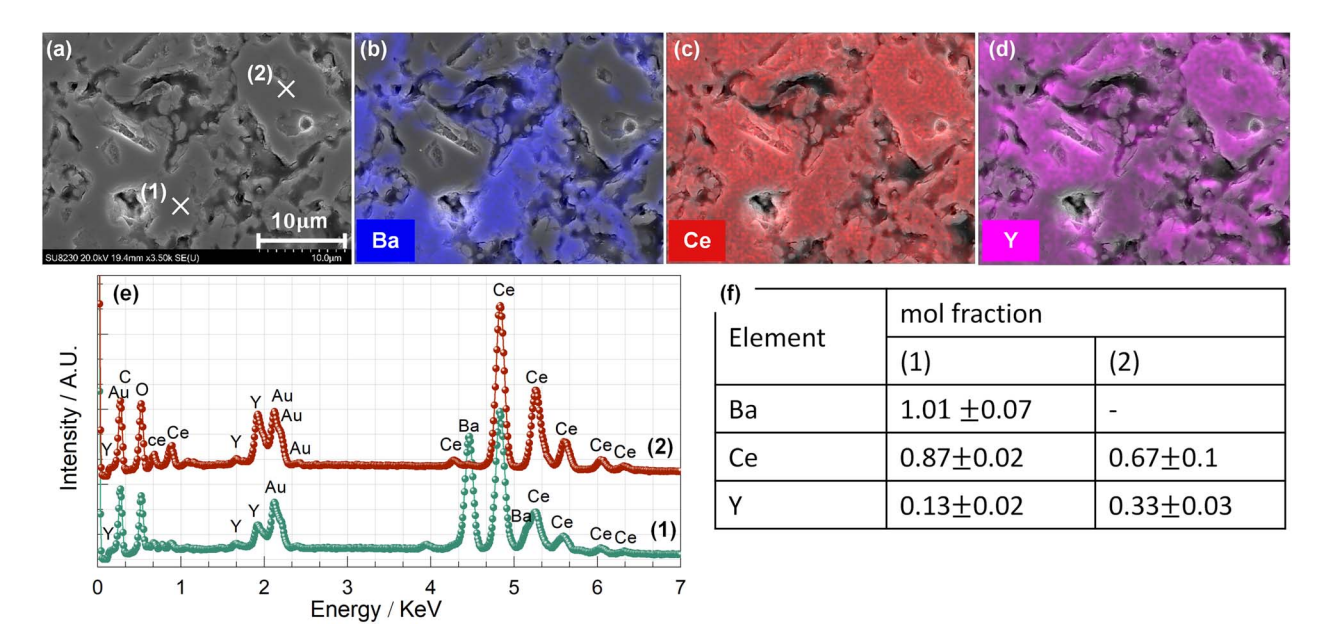


Fig. 7 Cation distribution in the BCY20-CYO20 (1:1 wt. ratio) co-ionic composite electrolyte, sintered at 1600 °C, analysed by SEM-EDS: SEM image (a), EDS maps (b-e), EDS spectrum (f), and semi-quantitative compositional analysis (g) for points (1) and (2), as marked in image (a). Stoichiometries are normalised such that the atomic fractions of Zr + Ce + Y sum to 1 for both the perovskite and fluorite phases. Cation distribution in the BCY20-CYO20 (1:1 wt. ratio) co-ionic composite electrolyte, sintered at 1600 °C, analysed by SEM-EDS: SEM image (a), EDS maps (b-d), EDS spectrum (e), and semi-quantitative compositional analysis (f) for points (1) and (2), as marked in image (a). Stoichiometries are normalised such that the atomic fractions of Zr + Ce + Y sum to 1 for both the perovskite and fluorite phases.

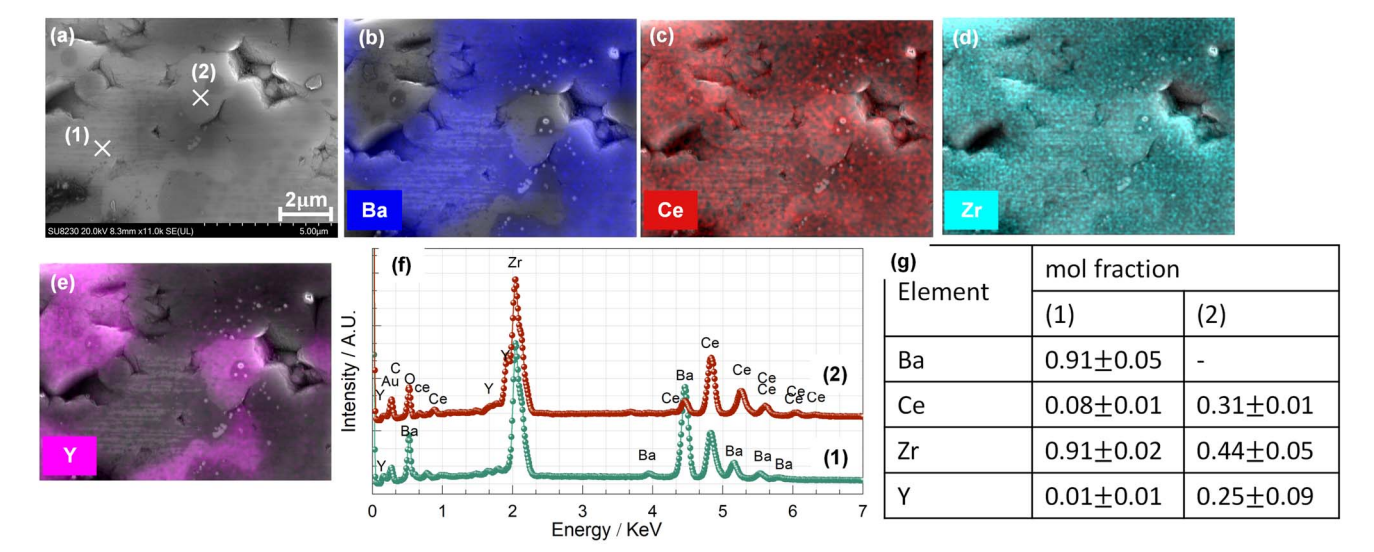


Fig. 8 Cation distribution in the BCY20-8YSZ (1:1 wt. ratio) co-ionic composite electrolyte, sintered at 1600 °C, analysed by SEM-EDS: SEM image (a), EDS maps (b-e), EDS spectrum (f), and semi-quantitative compositional analysis (g) for points (1) and (2), as marked in image (a). Stoichiometries are normalised such that the atomic fractions of Zr + Ce + Y sum to 1 for both the perovskite and fluorite phases.

effective acceptor concentration of BCY20 shows negligible change compared to the single phase, indicating limited cation diffusion between the two phases. However, for the higher annealing temperatures, particularly for the composite with 8YSZ, hydration of the perovskite phase is significantly reduced. In line with findings of XRD and microscopy, extensive interdiffusion in the BCY20-8YSZ at the higher temperatures results in a minor concentration of acceptor dopants in the proton conducting perovskite phase.

Fig. 9b and c also depict the effective acceptor concentration based on hydration, here for BZCY442 and BZY20, respectively, in composites with CYO20 and 8YSZ. Similar behaviours are observed; the effective acceptor concentration decreases with increasing annealing temperature, again the composites with 8YSZ exhibit very low hydration levels.

Finally, Fig. 9d displays the data for BZS20-CYO20 composites. The initial effective acceptor concentration of BZS20 is already low and decreases further in the composite. Due to this limited hydration behaviour, this composition was not investigated further in the present study.

All in all, at an annealing temperature of 1600 °C, only the BCY20-CYO20 composite remains within an acceptable acceptor level (10.3 mol%), likely preserving reasonable mixed ionic conductivity.

By constraining the annealing temperature to 1400 °C, the proton conducting phase in both the nominal BCY20-CGO20 and BZCY442-CYO20 compositions retains at least 10 mol% effective acceptor concentration, and shows acceptable ionic conductivity (e.g., $\sigma = 0.02 \text{ Scm}^{-1}$ for $BaZr_{0.44}Ce_{0.35}Y_{0.2}O_{3-\delta}$ compared to $\sigma = 0.01~{\rm Scm}^{-1}$ for ${\rm BaZr}_{0.5}{\rm Ce}_{0.4}{\rm Y}_{0.1}{\rm O}_{3-\delta}$ in humid O2 at 650 °C44). It is highlighted that the BCY20, BZCY442 and BZY20 phases all show low effective acceptor concentration when mixed with 8YSZ, even at an annealing temperature of 1200 °C. However, for BZY20-8YSZ, the drop in effective acceptor concentration is less pronounced compared to that of BCY20-8YSZ, BZCY442-8YSZ.

Based on the measured proton concentration, we take further the analysis by estimating the final composition of the proton conducting phase of the composite (Table 3). By way of example, the effective proton concentration after annealing of BCY20-CYO20 at 1600 °C is 10% (Fig. 9a). This corresponds to a 10% effective acceptor doping, i.e. $BaCe_{0.9}Y_{0.1}O_{2.95}$. By considering the molar ratio between the two phases (Table 1) and applying molar balance in the reaction, the final composition of the oxide-ion conducting phase can also be determined:

BaCe_{0.8}Y_{0.2}O_{2.9} + 2Ce_{0.8}Y_{0.2}O_{1.9}
$$\xrightarrow{T=1600 \text{ °C}}$$

$$BaCe_{0.9}Y_{0.10}O_{2.95} + 2Ce_{0.75}Y_{0.25}O_{1.9} \qquad (1)$$

For the BCY20-8YSZ co-ionic electrolyte, SEM-EDS analysis (Fig. 9) reveals zirconium diffusion from the fluorite phase into the perovskite phase. This is consistent with the thermodynamic stability of the BaZrO₃ phase discussed previously. Therefore, after annealing at 1400 °C and 1600 °C, the expected composition is BaCe_{0.8-x}Zr_{0.2+x}O₃. Based on the SEM-EDS data, the cerium content in the perovskite phase is measured to be approximately 0.08, yielding a final composition of BaCe_{0.08}Zr_{0.92}O₃:

$$BaCe_{0.8}Y_{0.2}O_{2.9} + 2.3Zr_{0.84}Y_{0.16}O_{1.94} \xrightarrow{T=1600 \, ^{\circ}C}$$

$$BaCe_{0.08}Zr_{0.92}O_{3} + 2.3Zr_{0.43}Ce_{0.31}Y_{0.25}O_{1.88} \qquad (2)$$

The persistence of significant interdiffusion even with Sc³⁺ - a dopant with minimal size mismatch in the perovskite lattice - suggests that size mismatch alone cannot explain the

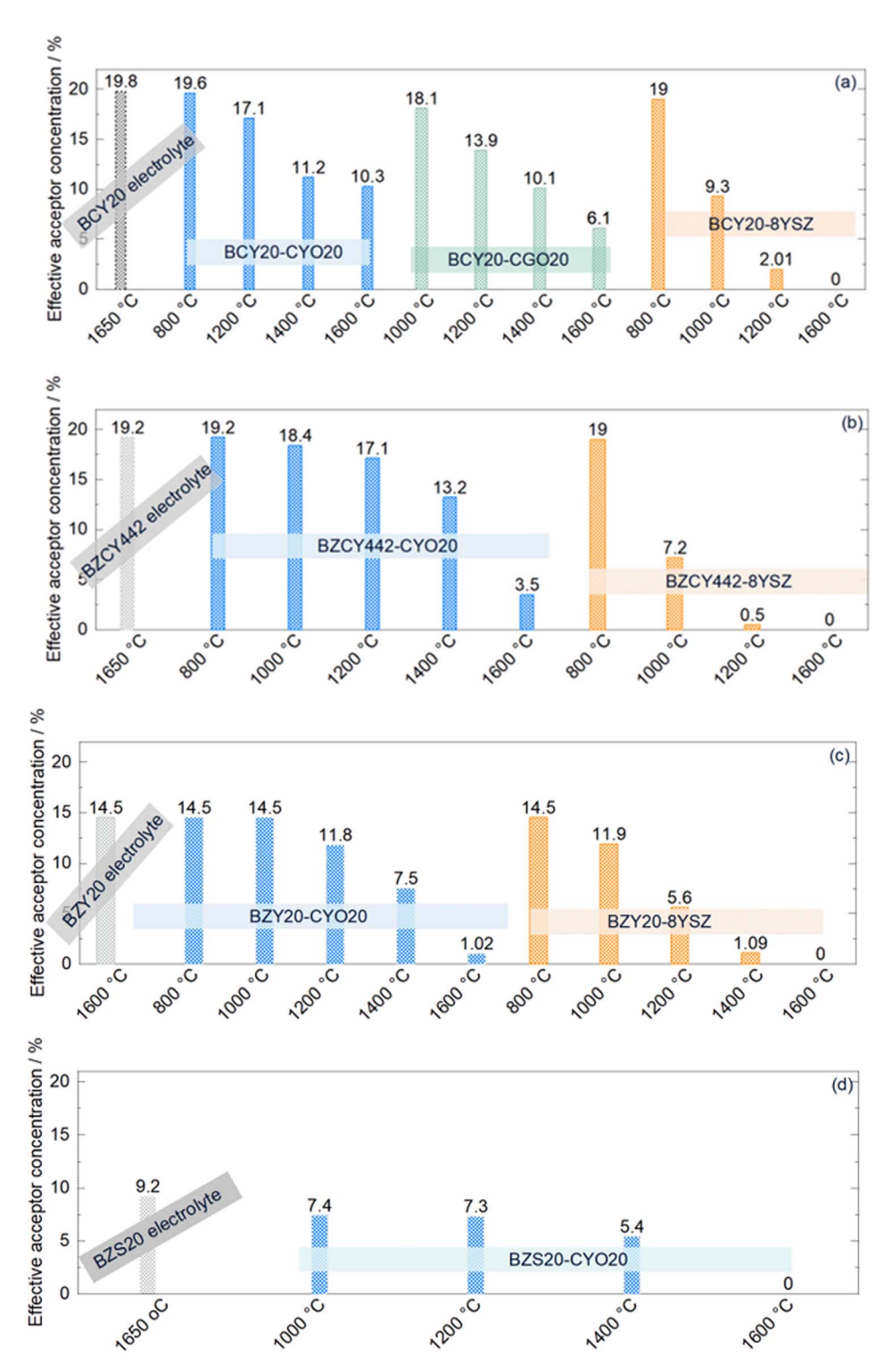


Fig. 9 Effective acceptor concentration of co-ionic electrolytes as a function of annealing temperature: BCY20 with CYO20, CGO20, and 8YSZ (a); BZCY442 with CYO20 and 8YSZ (b); BZY20 with CYO20 and 8YSZ (c); and BZS20 with CYO20 (d). Proton concentrations of the single-phase materials BCY20, BZCY442, BZY20, and BSZ20 are included as references. For fabrication methods and phase ratios, see Table 1. For composites sintered at lower temperatures (T < 1200 °C), the minor amount of surface water adsorbed by the oxide ion-conducting phases was subtracted from the relative weight change in the thermogravimetric data (see SI Section 8).

driving force for cation redistribution. Alternative mechanisms, such as differences in oxygen vacancy formation energies or the effects of lattice strain and coordination environments (CN = 6 in perovskite νs . CN = 8 in fluorite),

may be more influential. Moreover, lattice distortion induced by dopant incorporation – rather than size mismatch *per se* – has been identified as a critical factor influencing defect behaviour and ion mobility.⁴⁵

Table 3 Final composition and effective acceptor concentration ([Acc']eff) of the proton conducting phase in the composite co-ionic electrolyte after 10 h annealing at 1400 °C and 1600 °C, estimated from hydration and EDS results

Co-ionic electrolyte	Composition of proton conducting phase [Acc'] _{eff}				
	Based on hydration results	Based on EDS results			
	T = 1400 °C	<i>T</i> = 1600 °C	<i>T</i> = 1600 °C		
BCY20-CYO20	$BaCe_{0.89}Y_{0.11}O_{2.95}\\11.2\%$	$BaCe_{0.9}Y_{0.10}O_{2.95}\\10.3\%$	$\begin{array}{c} BaCe_{0.87}Y_{0.13}O_{2.94} \\ 13\% \end{array}$		
BCY20-CGO20	$BaCe_{0.9}Y_{0.1}O_{2.95}$ 10.1%	${\rm BaCe_{0.94}Y_{0.06}O_{2.94}} \\ {\rm 6.1\%}$	_		
BCY20-8YSZ	$BaCe_{0.8-x}Zr_{0.2+x}O_3$	$BaCe_{0.8-x}Zr_{0.2+x}O_3$	$\begin{array}{c} Ba_{0.9}Ce_{0.08}Zr_{0.91}\;Y_{0.02}O_{3}\\ 2\% \end{array}$		
BZCY442-CYO20	$\begin{array}{c} \text{BaZr}_{0.4}\text{Ce}_{0.47}\text{Y}_{0.13}\text{O}_{2.94} \\ 13.2\% \end{array}$	$\begin{array}{l} BaZr_{0.4}Ce_{0.56}Y_{0.04}O_{2.9} \\ 3.5\% \end{array}$	_		
BZCY442-8YSZ	$\begin{array}{c} \text{BaZr}_{0.6+x}\text{Ce}_{0.4-x}\text{O}_3 \\ 0 \end{array}$	$BaZr_{0.6+x}Ce_{0.4-x}O_3$			
BZY20-CYO20	$BaZr_{0.8}Ce_{0.12}Y_{0.08}O_{2.96}$ 7.5%	$\begin{array}{c} BaZr_{0.8}Ce_{0.19}Y_{0.01}O_{3} \\ 1.02\% \end{array}$			
BZY20-8YSZ	$BaZr_{0.99}Y_{0.01}O_3$ 1.09%	${}^{ ext{BaZr}_{0.8} ext{O}_3}_{ ext{0}}$			
BZS20-CYO20	$BaZr_{0.99}Sc_{0.05}O_{3} \\ 5.4\%$	${ m BaZrO_3} \ 0$			

The higher effective acceptor concentration ([Acc']eff) estimated by EDS compared to TG (e.g., 13 vs. 10.3 mol% for BCY20-CYO20, Table 3) indicates that the reduction in effective acceptor content is not solely attributable to diffusion into the

fluorite phase. It may also arise from an internal defect reaction within the perovskite lattice, whereby Ba vacancies (v''_{Ba}) generated either through interdiffusion with the fluorite phase or by Ba evaporation at elevated temperatures - induce the

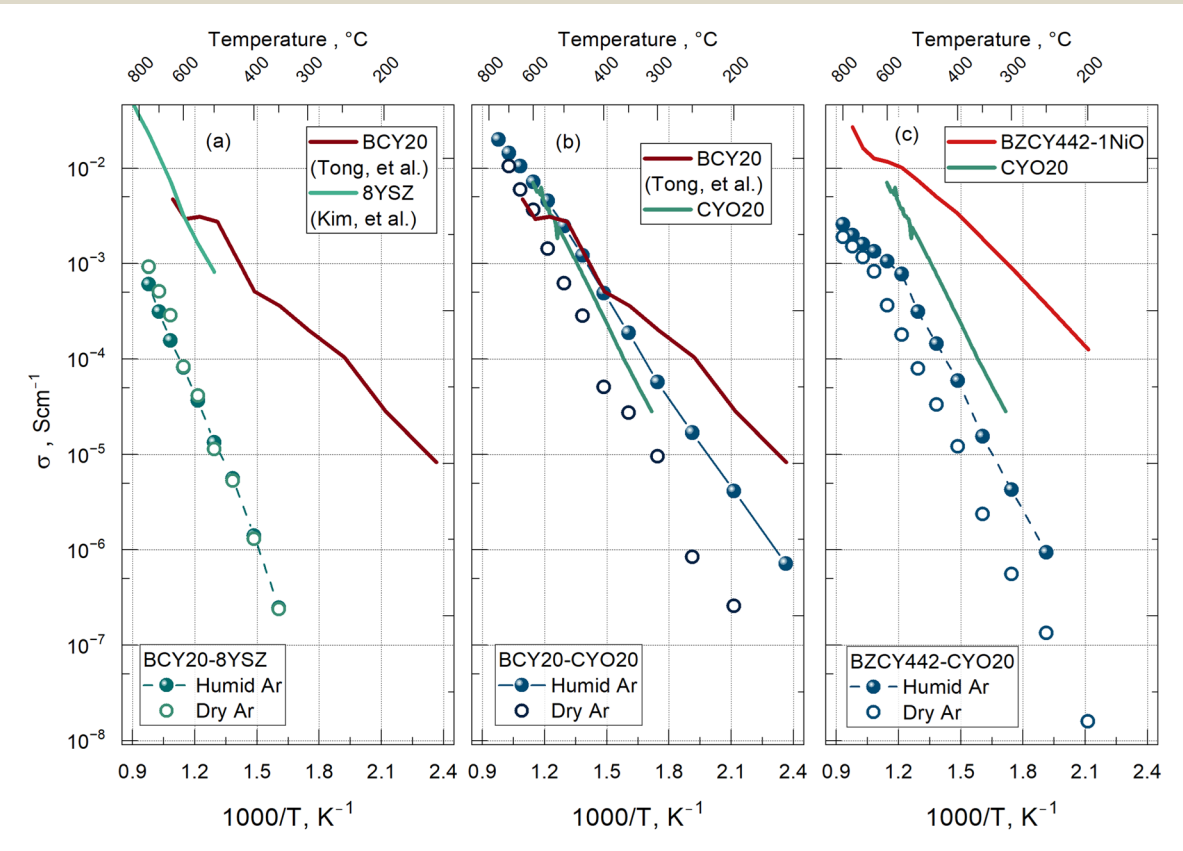


Fig. 10 DC conductivity of co-ionic electrolytes sintered at 1600 °C: BCY20-8YSZ (a), BCY20-CYO20 (b), BZCY442-CYO20 (c). Fabrication methods and phase compositions are detailed in Table 1. For comparison, the conductivities of single-phase electrolytes - 8YSZ,47 CYO20, BCY20,48 and BZCY442-1NiO - are also included.

relocation of trivalent acceptor dopants from the B-site. These dopants then might act as donor species, thereby reducing the effective oxygen vacancy concentration.^{23,46}

3.2.4 Electrical conductivity of the composite co-ionic electrolytes made by SSR. Fig. 10 presents the electrical conductivity of co-ionic electrolytes – BCY20–8YSZ (a), BCY20–CYO20 (b), and BZCY442–CYO20 (c) – sintered at 1600 °C *via* the SSR route as described in Table 1. Representative impedance spectra at both low and high temperatures (Fig. S13), along with bulk and grain boundary conductivities (Fig. S14) and activation energies (Tables S6 and S7) are provided in SI.

Among the examined samples, BCY20–8YSZ exhibits the lowest total conductivity ($\sigma = 0.00015~{\rm Scm^{-1}}$ at 650 °C), and shows negligible variation between dry and humid Ar, reflecting the absence of acceptor dopants in the perovskite phase (Fig. 7 or Table 3).

In contrast, BCY20–CYO20 demonstrates the highest conductivity in humid Ar. At 650 °C, the proton transport number is 0.7 ($\sigma_{\rm wet} = 0.01~{\rm Scm}^{-1}$ and $\sigma_{\rm dry} = 0.003~{\rm Scm}^{-1}$).

Although BCY20–CYO20 exhibits the highest total conductivity among the compositions studied, its high Ce content may compromise chemical stability in CO₂- and H₂O- rich environments, which are relevant for SOECs operation. In contrast, BZCY442–CYO20, despite its lower conductivity ($\sigma=0.002$ Scm⁻¹ at 650 °C), may offer enhanced stability under such operating conditions. Therefore, further long-term studies are necessary to evaluate the CO₂ tolerance and overall durability of these co-ionic electrolytes under realistic operating conditions.

Additionally, the conductivity of the BZYYb811–CGO20 coionic electrolyte sintered at 1600 °C via the SSRS route (Table 1) is provided in the SI. The BZYYb811–CGO20 co-ionic electrolyte exhibits poor conductivity (*e.g.*, at 650 °C, $\sigma = 0.0007$ Scm⁻¹) as expected from the cation distribution shown in Fig. 6.

This study highlights the critical role of cation selection in each phase in proton-oxide ion conducting composites and offers an explanation for the wide range of conductivity values reported in the literature (Table S1), such as 0.00006 Scm⁻¹ for $BaZr_{0.8}Y_{0.2}O_3-Y_{0.16}Zr_{0.84}O_{1.92}$ (ref. 49) and 0.01 Scm^{-1} BaCe_{0.8}Y_{0.2}O_{2.9}-Ce_{0.8}Y_{0.2}O_{1.9}.50 We demonstrated that the SSRS method may not be suitable for fabricating composite co-ionic electrolytes, as it results in insufficient acceptor doping in the perovskite phase and excessive doping in the fluorite phase (Fig. 6). In the SSR method we can instead combine the presynthesised phases directly into the desired composite and reduce the detrimental inter-diffusion between the two phases by selecting appropriate cations and controlling the sintering temperature (Fig. 7). The significant decrease in hydration and the large discrepancy in conductivity indicate rapid cation diffusion between the perovskite and fluorite phases. Thus, investigating the cation diffusion coefficient between these phases is recommended as future research.

4. Conclusions

This study has clarified the role of cation distribution in composite co-ionic electrolytes, which consist of proton conducting (BCY20, BZCY442, BZY20 or BZS20) and oxide-ion

conducting phases (CYO20, CGO20, or 8YSZ). The results show that both the annealing temperature and the specific cations used in each phase significantly impact electrolyte performance. Notably, the proton conducting phase often loses acceptor dopants, with zirconium frequently occupying the B-site, and higher annealing temperatures accelerate this cation redistribution.

Our hydration study proved to be an effective method for predicting the final cation distribution of the composites. It revealed that the effective acceptor concentration in the proton conducting phase decreases with increasing processing temperature, with a more pronounced decline in systems containing 8YSZ compared to those containing CYO20 or CGO20. After annealing above 1200 °C, the effective acceptor concentration becomes negligible in BCY20–8YSZ and BZCY442–8YSZ but remains at 10.3 mol% for BCY20–CYO20 even after annealing at 1600 °C.

The lowest performance of the co-ionic electrolytes, marked by poor hydration and conductivity, was observed in systems where 8YSZ was employed as the oxide-ion conductor *e.g.*, BCY20–8YSZ ($\sigma=8\times10^{-5}~\rm Scm^{-1}$ at 650 °C). This was due to zirconium diffusion into the perovskite phase being counteracted by yttrium diffusion into the fluorite phase, resulting in a dopant-deficient proton conducting phase and an over-doped oxide ion conducting phase. Conversely, the best performance of the co-ionic electrolytes – exhibiting a hydration degree above 50% and acceptable ionic conductivity in wet Ar – was achieved when CGO20 or CYO20 served as the oxide-ion conductor (*e.g.*, $\sigma=0.01~\rm Scm^{-1}$ at 650 °C in wet Ar for BCY20–CYO20). These composite materials are therefore recommended for use in co-ionic solid oxide electrochemical cells.

Author contributions

A. M. D.: conceptualization, all experiments, writing the original draft; L. A.: conducting conductivity measurements of the fluorite phase, reviewing, and editing; S. E.: reviewing and editing; B. J.: TOPAS fitting, reviewing, and editing; P. A. C.: STEM/EDS work, reviewing and editing; J. M. S.: project administration, reviewing and editing; R. H.: reviewing and editing; T. N.: conceptualization, supervision, reviewing, editing, and finalizing the manuscript. All authors contributed to scientific discussions.

Conflicts of interest

There are no conflicts to declare.

Data availability

Supplementary information: the data supporting this article have been included as part of the SI. See DOI: https://doi.org/10.1039/d5ta02711j.

Acknowledgements

This project has received European Union's Horizon 2020 research and innovation funding under grant agreement No. 838077. The Research Council of Norway is acknowledged for support to the Norwegian Center for Transmission Electron Microscopy (NORTEM) national infrastructure project 197405. The authors acknowledge the ESRF for provision of synchrotron radiation facilities under proposal number A31-1-270 and we would like to thank Wouter van Beek and Kenneth Marshall for assistance and support in using beamline BM31 (SNBL). The authors also thank Daniel Irving at the I15-1 beamline at the Diamond Light Source, UK, for synchrotron X-ray measurements.

References

- 1 K.-Q. Zheng, M. Ni, Q. Sun and L.-Y. Shen, *Acta Mech. Sin.*, 2013, 29, 388–394.
- 2 J. Cao, C. Su, Y. Ji, G. Yang and Z. Shao, J. Energy Chem., 2021, 57, 406–427.
- 3 H. Iwahara, T. Yajima, T. Hibino and H. Ushida, *J. Electrochem. Soc.*, 1993, 140, 1687.
- 4 J. Huang, J. Yuan, Z. Mao and B. Sundén, ASME. J. Fuel Cell Sci. Technol., 2010, 7, 011012.
- 5 Y.-T. Lu, W.-C. Huang, S.-H. Wang, T.-C. Chen and H.-Y. Chang, *Int. J. Hydrogen Energy*, 2024, **54**, 176–188.
- 6 N. Bausa, S. Escolastico and J. M. Serra, J. CO₂ Util., 2019, 34, 231–238.
- 7 L. Gan, L. Ye, S. Wang, M. Liu, S. Tao and K. Xie, *Int. J. Hydrogen Energy*, 2016, **41**, 1170–1175.
- 8 T. Norby, in *Perovskite Oxide for Solid Oxide Fuel Cells*, Springer, 2009, pp. 217–241.
- 9 G. Zhou, Y. Li, Y. Luo, W. Huang and B. Li, *Ceram. Int.*, 2023, **49**, 11184–11196.
- 10 M. A. Azimova and S. McIntosh, *Solid State Ionics*, 2009, **180**, 160–167.
- 11 Y. Nigara, K. Yashiro, T. Kawada and J. Mizusaki, *Solid State Ionics*, 2003, **159**, 135–141.
- 12 J. Huang, L. Zhang, C. Wang and P. Zhang, *Int. J. Hydrogen Energy*, 2012, 37, 13044–13052.
- 13 D. Medvedev, E. Pikalova, A. Demin, A. Podias, I. Korzun, B. Antonov and P. Tsiakaras, *J. Power Sources*, 2014, 267, 269–279.
- 14 D. Medvedev, V. Maragou, E. Pikalova, A. Demin and P. Tsiakaras, *J. Power Sources*, 2013, 221, 217–227.
- 15 Z. Zhao, M. Zou, H. Huang, H. Wofford and J. Tong, *Ceram. Int.*, 2021, 47, 32856–32866.
- 16 K. Kreuer, Annu. Rev. Mater. Res., 2003, 33, 333-359.
- 17 D. Clark, H. Malerød-Fjeld, M. Budd, I. Yuste-Tirados, D. Beeaff, S. Aamodt, K. Nguyen, L. Ansaloni, T. Peters and P. K. Vestre, *Science*, 2022, 376, 390–393.
- 18 K. Taghikhani, A. Dubois, J. R. Berger, S. Ricote, H. Zhu and R. J. Kee, *Membranes*, 2021, **11**, 378.
- 19 K.-Y. Park, T.-H. Lee, S. Jo, J. Yang, S.-J. Song, H.-T. Lim, J. H. Kim and J.-Y. Park, *J. Power Sources*, 2016, 336, 437–446.

- 20 M. E. Ivanova, S. Escolástico, M. Balaguer, J. Palisaitis, Y. J. Sohn, W. A. Meulenberg, O. Guillon, J. Mayer and J. M. Serra, Sci. Rep., 2016, 6, 34773.
- 21 I. Hasle, S. P. Waldow, U. N. Gries, R. A. De Souza, E. Vøllestad and R. Haugsrud, *J. Mater. Chem. A*, 2021, 9, 21142–21150.
- 22 M. Price, J. Dong, X. Gu, S. A. Speakman, E. A. Payzant and T. M. Nenoff, *J. Am. Ceram. Soc.*, 2005, **88**, 1812–1818.
- 23 A. M. Dayaghi, J. M. Polfus, R. Strandbakke, A. Pokle, L. Almar, S. Escolástico, E. Vøllestad, J. M. Serra, R. Haugsrud and T. Norby, *Solid State Ionics*, 2023, 401, 116355.
- 24 Y. Yamazaki, C.-K. Yang and S. M. Haile, *Scr. Mater.*, 2011, 65, 102–107.
- 25 A. M. Dayaghi, R. Haugsrud, M. Stange, Y. Larring, R. Strandbakke and T. Norby, *Solid State Ionics*, 2021, 359, 115534.
- 26 F. Iguchi, N. Sata, T. Tsurui and H. Yugami, Solid State Ionics, 2007, 178, 691–695.
- 27 J. Zhang, C. Ke, H. Wu, J. Yu, J. Wang and Y. Wang, J. Alloys Compd., 2017, 718, 85–91.
- 28 V. Grover and A. Tyagi, *J. Solid State Chem.*, 2004, **177**, 4197–4204.
- 29 J. Zamudio-García, J. M. Porras-Vázquez, A. Cabeza, J. Canales-Vázquez, E. R. Losilla and D. Marrero-López, ACS Appl. Mater. Interfaces, 2024, 16, 42198–42209.
- 30 P. Arunkumar, M. Meena and K. S. Babu, *Nanomater. Energy*, 2012, 1, 288–305.
- 31 X. Sun, J. Gu, D. Han and T. Norby, *Phys. Chem. Chem. Phys.*, 2022, **24**, 11856–11871.
- 32 K. H. Ryu and S. M. Haile, *Solid State Ionics*, 1999, **125**, 355–367.
- 33 T. Norby, M. Widerøe, R. Glöckner and Y. Larring, *Dalton Trans.*, 2004, 3012–3018.
- 34 A. Løken, T. S. Bjørheim and R. Haugsrud, *J. Mater. Chem. A*, 2015, 3, 23289–23298.
- 35 T. Norby, Nature, 2001, 410, 877.
- 36 Y. Larring and T. Norby, *Solid State Ionics*, 1995, 77, 147–151.
- 37 D. S. Tsvetkov, V. V. Sereda, D. A. Malyshkin, A. L. Sednev-Lugovets, A. Y. Zuev and I. L. Ivanov, *Chim. Techno Acta*, 2020, 7, 42–50.
- 38 M. Gonçalves, P. Maram, R. Muccillo and A. Navrotsky, *J. Mater. Chem. A*, 2014, 2, 17840–17847.
- 39 A. K. Andersson, S. M. Selbach, C. S. Knee and T. Grande, *J. Am. Ceram. Soc.*, 2014, **97**, 2654–2661.
- 40 D. Han, M. Majima and T. Uda, *J. Solid State Chem.*, 2013, 205, 122-128.
- 41 K. Takeuchi, C.-K. Loong, J. Richardson Jr, J. Guan, S. Dorris and U. Balachandran, *Solid State Ionics*, 2000, **138**, 63–77.
- 42 C.-K. Loong, M. Ozawa, K. Takeuchi, K. Ui and N. Koura, *J. Alloys Compd.*, 2006, **408**, 1065–1070.
- 43 J. Lagaeva, D. Medvedev, A. Demin and P. Tsiakaras, *J. Power Sources*, 2015, **278**, 436–444.
- 44 K. Leonard, Y.-S. Lee, Y. Okuyama, K. Miyazaki and H. Matsumoto, *Int. J. Hydrogen Energy*, 2017, 42, 3926–3937.
- 45 D. S. Aidhy, B. Liu, Y. Zhang and W. J. Weber, *Comput. Mater. Sci.*, 2015, **99**, 298–305.

- 46 J. M. Polfus, M.-L. Fontaine, A. Thøgersen, M. Riktor, T. Norby and R. Bredesen, *J. Mater. Chem. A*, 2016, 4, 8105–8112.
- 47 S. K. Kim, H. J. Lee, J. Y. Moon, Y.-R. Jo, J. Lee, J.-H. Park, S.-D. Kim and J. H. Joo, *J. Mater. Chem. A*, 2024, **12**, 8319–8330.
- 48 J. Tong, D. Clark, L. Bernau, A. Subramaniyan and R. O'Hayre, *Solid State Ionics*, 2010, **181**, 1486–1498.
- 49 X. Luo, B. Meng, M. Zhao, H. Xie, L. Bian and X. Yang, *Ionics*, 2019, **25**, 1157–1165.
- 50 Y. Liu, L. Dai, W. Zhang, H. Zhou, Y. Li and L. Wang, *Ceram. Int.*, 2016, **42**, 6391–6398.